REPORT DOCUMENTATION PAGE

1. REPORT DATE (DD-MM-YYYY)	2. REPORT TYPE	3. DATES COVERED (From - To)
02-03-2010	Final Performance Report	Nov 06 - Nov 09

4. TITLE AND SUBTITLE
Aero-Optical Investigation of a Pod Directed Energy System

5a. CONTRACT NUMBER
N00014-07-1-0291

5b. GRANT NUMBER

5c. PROGRAM ELEMENT NUMBER

6. AUTHOR(S)
Eric J Jumper

5d. PROJECT NUMBER
07PR03523-00

5e. TASK NUMBER

5f. WORK UNIT NUMBER

7. PERFORMING ORGANIZATION NAME(S) AND ADDRESS(ES)
DR. ERIC J. JUMPER
UNIVERSITY OF NOTRE DAME
110 HESSERT LABORATORY
NOTRE DAME, IN 46556-5612

8. PERFORMING ORGANIZATION REPORT NUMBER

9. SPONSORING/MONITORING AGENCY NAME(S) AND ADDRESS(ES)
Quentin Saulter
Office of Naval Research
875 North Randolph Street
Arlington, VA 22203-1995

10. SPONSOR/MONITOR'S ACRONYM(S)

11. SPONSOR/MONITOR'S REPORT NUMBER(S)
ONR 351

12. DISTRIBUTION/AVAILABILITY STATEMENT
Unlimited.

13. SUPPLEMENTARY NOTES

14. ABSTRACT
This report covers the work performed under ONR Grant number N00014-07-1-0291, entitled "Aero-Optical Investigation of a Pod Directed Energy System." As described herein, the initial effort investigated approaches to using passive flow control to mitigate the presence of shocks over the exit pupil of a relatively large aperture laser beam projected from an underbody pod for an F/A-18 aircraft up to flight Mach numbers of Mach 0.8, and still provide a large field of regard. During the course of the investigation, the Grant Technical Manager redirected our efforts toward studying the aero-optical environment imposed on a laser beam projected from a turret placed underneath a helicopter. The results of both of these studies presented in this report.

15. SUBJECT TERMS

16. SECURITY CLASSIFICATION OF:			17. LIMITATION OF ABSTRACT	18. NUMBER OF PAGES	19a. NAME OF RESPONSIBLE PERSON
a. REPORT	b. ABSTRACT	c. THIS PAGE			Michael A. Zenk
Unclas	Unclas	Unclas	UU	33	19b. TELEPHONE NUMBER (Include area code) 574-631-3755

Final Report

to

Office of Naval Research

for

Grant Number N00014-07-1-0291

Aero-Optical Investigation of a Pod Directed Energy System

Eric J. Jumper, Professor
and
R. Mark Rennie, Research Assistant Professor

Department of Aerospace and Mechanical Engineering
University of Notre Dame
Notre Dame, IN 46556

28 February 2010

Abstract

This report covers the work performed under ONR Grant number N00014-07-1-0291, entitled "Aero-Optical Investigation of a Pod Directed Energy System." As described herein, the initial effort investigated approaches to using passive flow control to mitigate the presence of shocks over the exit pupil of a relatively large aperture laser beam projected from an underbody pod for an F/A-18 aircraft up to flight Mach numbers of Mach 0.8, and still provide a large field of regard. During the course of the investigation, the Grant Technical Manager redirected our efforts toward studying the aero-optical environment imposed on a laser beam projected from a turret placed underneath a helicopter. The results of both of these studies presented in this report.

I. Introduction

Over the course of approximately four decades of developing high-energy laser systems as speed-of-light weapon systems for destroying targets at large distances, investigators have learned to deal with the aberrating effects of the atmosphere. These effects are imposed by density fluctuations associated with atmospheric turbulence in regions of the lasers propagation path where temperature gradients are also present. At any given altitude, the pressure along the temperature-gradient, turbulent air is essentially constant in time, so that the density fluctuations of the air are due to the temperature fluctuations via the perfect gas law. Since the index of refraction of air in the ranges of laser wavelengths of interest is directly proportional to the density of the air, these temperature fluctuations cause index-of-refraction fluctuations along the laser's path that range in scale size over the beam's diameter and are time varying due to the natural convection of these turbulent structures by atmospheric winds and by the fact that the laser beam may be sluing through the air as it tracks the target. Not only has an entire mathematical approach been developed for dealing with the aberrating environment imposed by atmospheric turbulence, but methods for mitigating its aberrating effects have been developed through adaptive optics. This analysis and mitigation schemes have been applied to laser systems that are both ground based and airborne. However, an often overlooked effect on airborne laser systems is the aberrating environment imposed by the air flow over and around an airborne platform used to carry the laser system; this latter effect is referred to as the aero-optical problem. Aero-optical effects range from the pseudo-stationary density variation caused by high-speed flow over the exit pupil of the laser where the flow is caused to accelerate and decelerate as it moves over the shape of the pupil, which is often spherical, to the creation of shocks when the air reaches Mach one as it is accelerated above the flight Mach number to the effect of turbulence in the boundary layer and separated flows [1-6]. These aero-optical effects are mainly applicable to airborne platforms that have relatively high flight velocities, like, for example, an F/A-18, transonic fighter; but, for a propeller-driven or rotory-wing aircraft, prop wash creates severe aberrating flow environment if the laser is to be propagated through it.

Although the original intent of this grant was to study only the aero-optical effects associated with transonic flight and the aero-optic environment imposed on the exit pupil of a laser in an underbody, centerline pod on an F/A-18, due to redirection by the program Technical Manager, this grant effort ended up study, not only the transonic problem but also rotory-wing problem as well. In addition, some of our effort was directed toward developing a new high-speed wavefront sensor, but little mention of this portion of the work will be included in this report, other than a very brief description of the work at the end of the report. Because the main interest in the work has now shifted to the rotory-wing problem, this work will be presented first, followed by the work on the F/A-18 laser pod.

II. Rotory-Wing Aircraft Aero-Optics

A. Introduction

For helicopter-mounted optical systems, the flight speed of the aircraft platform is in most cases, incompressible; as such, aero-optic aberrations are expected to originate primarily from the helicopter blades which can have tip speeds up to Mach 1 in some parts of the flight envelope. Evaluating the aero-optic environment in the vicinity of the helicopter therefore depends upon an understanding of the blade wake and tip-vortex dynamics and its associated aero-optic aberrations. An understanding of the character of the helicopter gross flow field is also needed in order to determine the location of the blade wake system as a function of helicopter flight regime. To our knowledge, no such investigation has been previously performed.

B. Approach

The fluid mechanics of wing-tip vortices has been studied extensively in the past since they dominate the wakes of lifting vehicles and have a direct impact on aircraft spacing near airports [7-11]. These studies show that the tip-vortex flow field consists of a rotational core surrounded by a non-rotational outer region. The core region of the vortex may also contain either jet-like or wake-like axial velocity components depending on the particular origin and history of the vortex. Since the total pressure is nearly constant across the vortex profile, the large flow velocities (both axial as well as azimuthal) close to the vortex core result in a significant reduction in static pressure at the center of the vortex; it is this reduced static pressure at the center of the vortex, with concomitant reductions in density and index-of-refraction, that result in the aero-optic aberrations produced by a tip vortex. Although the global wake structure for a helicopter may be significantly different from that of a fixed-wing aircraft (i.e. helical tip vortex pattern versus a linear one), the flow field for a single tip vortex is essentially the same, with vortices shed from both types of aircraft showing good agreement with, for example, the Lamb-Oseen vortex model.

The kinds of tip-vortex aero-optic aberrations described above are considered to be fluid mechanic in origin in the sense that index-of-refraction variations ultimately originate from the velocity field of the tip vortex. As shown in [12], at low-convective Mach numbers, the velocity field is unaffected by the thermodynamic properties of the flow. In this case, an existing empirical or experimental velocity field can be used to determine the pressure, temperature, and density fields which are used to calculate the optical aberrations induced by the flow. A fluid-dynamic model that performs this computation, called the weakly compressible model (WCM), has been developed previously at the University of Notre Dame [13], and is outlined in the following brief description.

The WCM is designed to compute pressure, temperature, and density fields from a pre-determined velocity field for "weakly compressible" flows in which development of the velocity field can be assumed to be decoupled from thermodynamic properties. The model is composed of the unsteady Euler equations, an isentropic temperature relation, and the ideal gas law:

$$\frac{Du}{Dt} = \frac{\partial u}{\partial t} + u\frac{\partial u}{\partial x} + v\frac{\partial u}{\partial y} + w\frac{\partial u}{\partial z}$$

$$\frac{Dv}{Dt} = \frac{\partial v}{\partial t} + u\frac{\partial v}{\partial x} + v\frac{\partial v}{\partial y} + w\frac{\partial v}{\partial z} \qquad (1)$$

$$\frac{Du}{Dt} = \frac{\partial w}{\partial t} + u\frac{\partial w}{\partial x} + v\frac{\partial w}{\partial y} + w\frac{\partial w}{\partial z}$$

Where u, v, and w are the Cartesian components of velocity in the x, y and z directions and t is time. The pressure gradients can then be calculated using Euler's equation

$$\frac{\partial P}{\partial x} = -\rho\frac{Du}{Dt}$$

$$\frac{\partial P}{\partial y} = -\rho\frac{Dv}{Dt} \qquad (2)$$

$$\frac{\partial P}{\partial z} = -\rho\frac{Dw}{Dt}$$

Where P is the pressure and ρ is the density. The solution is started by setting the initial guess for the pressure field as $p(x,y,z) = p_\infty$, after which Eqs. (1) to (4) are iterated to convergence. The initial adiabatic temperature distribution, T_{AB}, is computed using an assumed initial constant total temperature, T_T, throughout the flow field. The final T_T distribution of the converged solution can, however, vary throughout the flow field due to local unsteady pressure variations.

$$T_s = T_{Ad}\left(\frac{P}{P_\infty}\right)^{\frac{\gamma-1}{\gamma}} \qquad (3)$$

$$P = \rho R T_S \qquad (4)$$

In Eq. (3), T_S is the static pressure and the adiabatic temperature distribution, T_{Ad}, is determined at each point in the field using the velocity field by Eq. (5), where V is the scalar velocity made up of the three velocity components, and C_p is the specific heat at constant pressure of the air. Once the density field has been determined using the WCM, the index of refraction, n, at each point in the flow is determined using Eq. (6).

$$T_{Ad} = T_o - \frac{V^2}{2C_p} \qquad (5)$$

$$n(x,y,z) = 1 - K_{GD}\rho(x,y,z) \qquad (6)$$

K_{GD} is the Gladstone-Dale constant for a 1 μm wavelength in air, $K_{GD} = 2.25 \times 10^{-3}$ kg/m^3. Finally, the optical path difference, OPD, at each point in thelaser beam (x,y of its wavefront) passing through the index-of-refraction field in the y-direction of propagation is given by:

$$OPD = OPL - \overline{OPL} \tag{7}$$

$$OPL = \int n(t, x, y, z)dy \tag{8}$$

The approach for the present study was to determine aero-optic aberrations for realistic tip-vortex flows using the WCM in conjunction with empirical or experimental data for vortex velocity fields. As mentioned above, the resulting aero-optic data can be considered to be fluid mechanic in origin. Thermal aberrations could also be produced if temperature variations in the flow produced significant index-of-refraction gradients; such thermal aberrations would result, for example, if the helicopter engine exhaust were convected into the line of sight of the helicopter-mounted optical system. Effective treatment of such thermal aberrations requires, however, detailed computation or measurement of the flow and sources of heat around the helicopter and is beyond the scope of the present study.

C. Results

Example of Aero-Optic Aberrations Due to a Tip Vortex. Since wing-tip vortex flow fields are self-similar and compressibility effects on the flow field are small, the aero-optic character of a wing-tip vortex was estimated using the WCM in conjunction with a flow field that was scaled from subsonic measurements [14]. These measurements were performed on an unswept wing with a NACA 0012 profile, a chord of 0.127 m, and an aspect ratio of 8. At a distance of four chords downstream of the trailing edge of the wing, three component hot-wire measurements were made over a grid of 0.076 x 0.076 meters in 0.0025 meter increments in the y and z directions. This velocity field was then normalized by the freestream velocity and then scaled to different freestream Mach numbers. Figure 1 shows the velocity field obtained from hot wire measurements and the corresponding vorticity contours.
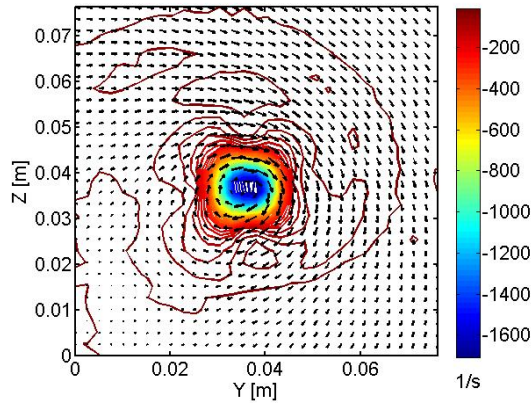

Figure 1. Velocity field for a wing tip vortex at 4 chord lengths downstream of the wing tip [14].

In Fig. 2, below, the experimental velocity field is compared to an estimate of the velocity field produced using the Lamb-Oseen model [11, 15]:

$$V_\theta(\bar{r}) = \frac{\Gamma}{2\pi r_c \bar{r}}\left(1 - e^{-\alpha\bar{r}^2}\right) \quad (9)$$

$$V_x = -\frac{A}{x}e^{-\alpha\bar{r}^2} \quad (10)$$

As shown by Eqs. (9) and (10), the velocity field of the Lamb-Oseen tip vortex is determined by the vortex core radius (r_c), the circulation (Γ), and the strength of the wake axial velocity profile , A; in Fig. 2, these parameters were selected to match the experimental data. Figure 2 shows that the experimental data can be reasonably-well characterized by the Lamb-Oseen model.
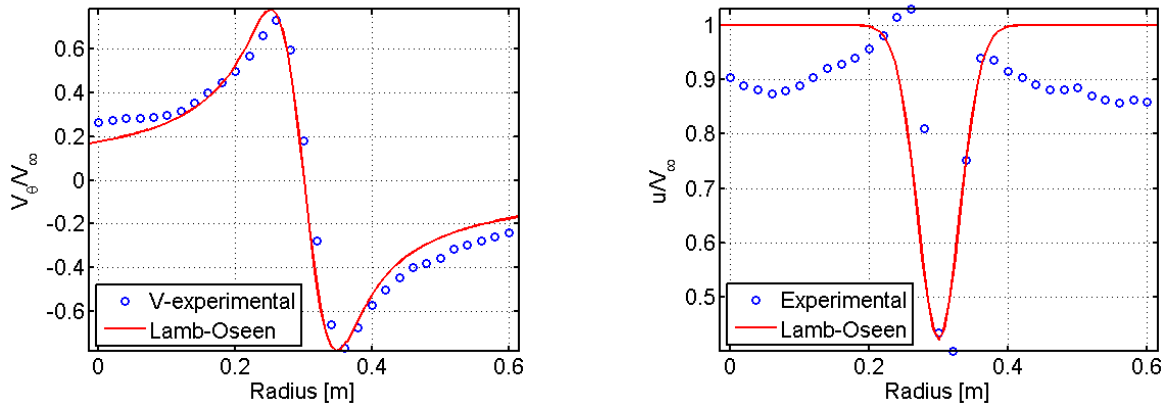

Figure 2. Comparison of Lamb-Oseen vortex model with three-component hotwire data [14].

The experimental velocity field was next scaled to different Mach numbers. The pressure and temperature fields, as well as the aero-optic aberration associated with this scaled experimental velocity field were computed using the WCM, shown in Figs. 3 and 4 for M = 0.3. As shown in Fig. 4, the peak-to-peak difference in OPD due to the M = 0.3 vortex aberration is 0.25 μm. This aberration would have a significant impact on a 1 μm wavelength beam of light that traversed the vortex flow field. It should be noted, however, that the results shown in Figs. 3 and 4 are for a relatively small tip vortex produced by a wing with a 0.127 m chord at M = 0.3. The aberrations produced by full-scale helicopter blade with significantly larger length scales, aerodynamic loading, and Mach number could produce significantly larger aberrations. Relations to scale the reduced-scale experimental to full-scale results are developed in the following section.
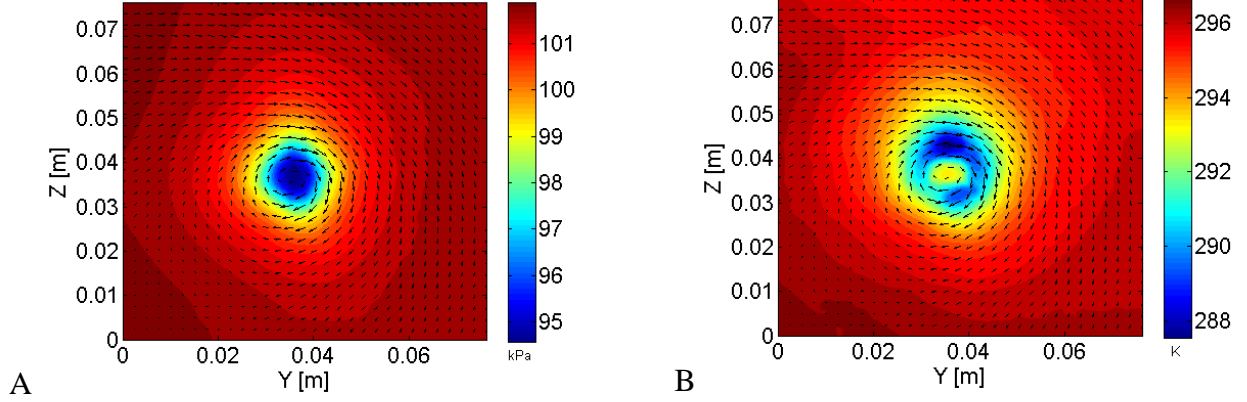
Figure 3. Pressure (A) and temperature (B) fields computed using the WCM for an experimental tip-vortex velocity field scaled to M=0.3.
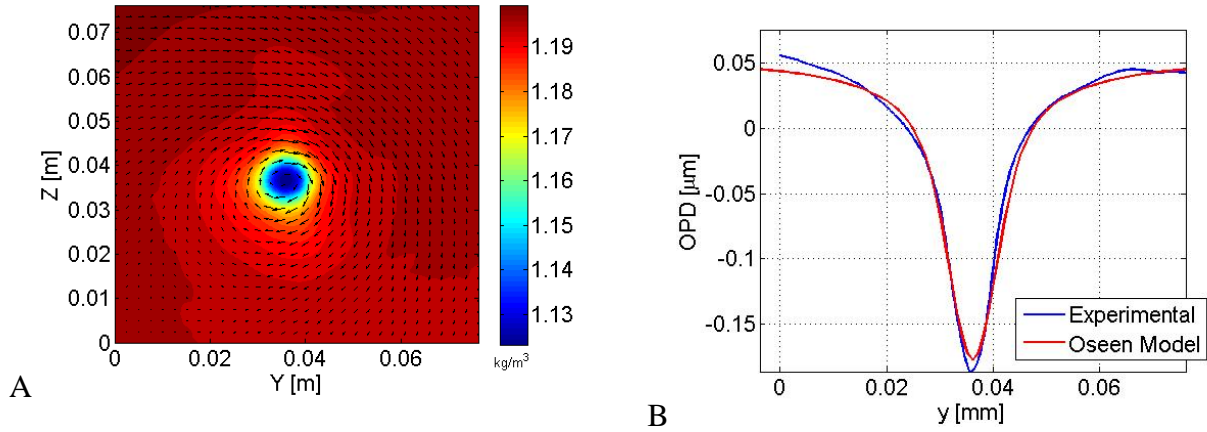

Figure 4. (A) WCM-computed density field for scaled experimental tip-vortex data and, (B) the corresponding OPD for the experimental data and the Lamb-Oseen model.

Scaling Relations. Scaling relations for the optical aberrations due to a tip vortex are developed from the Euler equations. The flow is assumed to have no radial velocity component and to be axisymmetric about the center of the core:

$$\frac{V_\theta}{r} = \frac{1}{\rho}\frac{\partial P}{\partial r}$$

$$V_x \frac{\partial V_x}{\partial x} = -\frac{1}{\rho}\frac{\partial P}{\partial x} \qquad (11)$$

$$\frac{\partial P}{\partial \theta} = 0$$

Dimensional analysis of Eq. (11) shows that the pressure gradient in the radial direction is approximately an order of magnitude larger than the pressure gradient in the streamwise direction [15]. As such, if the axial flow equation (second equation in Eq. (11)) is neglected, then inserting Eq. (9) into Eq. (11) gives:

$$\frac{\Gamma^2}{4\pi r^2}\left(1 - e^{-2\alpha\left(\frac{r}{r_c}\right)^2}\right) = \frac{1}{\rho}\frac{\partial P}{\partial r} \tag{12}$$

For isentropic flow, the right hand side of Eq. (12) becomes:

$$\frac{1}{\rho}\frac{\partial P}{\partial r} = \frac{\gamma RT}{\rho}\frac{\partial \rho}{\partial r} \tag{13}$$

Substituting Eq. (13) into Eq. (12) and integrating to obtain the density, then computing the index-of-refraction (Eq. (6)) and integrating as shown in Eq. (8), the OPD_{RMS} is seen to scale as:

$$OPD_{RMS} \approx \left(\frac{\rho}{\rho_{SL}}\right)\frac{\Gamma^2}{a^2 r_c} \tag{14}$$

where **a** is the speed of sound. OPD_{RMS} in this case is defined for a beam propagated normal to and centered on the vortex and is computed by the square root of the sum of the squares of the OPD at each position over the aperture of the beam; it is proportional because the actual OPD_{RMS} will depend on the ratio of the aperture of the beam to the vortex core radius, which will be addressed below. Assuming that the circulation of the vortex is equal to the circulation associated with the wing lift and the lift coefficient is uniform over the entire span, the scaling relation, Eq. (14), can also be expressed as:

$$OPD_{RMS} \approx \left(\frac{\rho}{\rho_{SL}}\right)\frac{C_l^2 M^2 c^2}{r_c} \tag{15}$$

Where C_l is the lift coefficient of the wing/rotor section, M is the Mach number, i.e., V/a, of the wing/blade at that point, and c is its chord. Based on this scaling, the spatial OPD_{RMS} is a function of the lift coefficient, Mach number, chord length, and vortex core radius. This indicates that if the lift from the wing decreases, so will the OPD_{RMS}, eventually going to zero as the lift goes to zero. Furthermore, the same Mach number squared relationship found in boundary layer experiments [16] is also obtained, and once again as the wing/rotor Mach number goes to zero so does the OPD_{RMS}. Finally, if the vortex diffuses due to viscous effects as predicted in the Lamb-Oseen model, or if vortex breakdown occurs, then Eq. (15) shows that the resulting increase in the core radius of the vortex produces a reduction in the overall spatial OPD_{RMS}.

The scaling relation shown in Eq. (14) or (15) were developed from an analysis of basic fluid-mechanic equations, similar to [17] which was used to explain rings in shadowgraphs created from tip vortices. To investigate this relationship, a data base of the optical aberrations for a range of tip-vortex parameters was generated. These data were created by generating velocity fields using the Lamb-Oseen model (Eqs. (9) and (10)) for different circulation strengths and core radii, determining the associated index-of refraction field using the WCM, and computing the spatial OPD_{RMS} associated with a collimated beam that traverses the flow field.

Optical data were also generated, in a similar way, by scaling the experimental flow field of [14] to different Mach numbers. Figure 5A shows these data plotted as a function of Mach number. In Fig. 5B, the same data are plotted as a function of the scaling parameter $(\rho/\rho_{sl})\,\Gamma/a^2 r_c$ shown in Eq. (14); Fig. 5B shows that this scaling parameter successfully collapses the data onto a single curve. For the experimental data, the density ratio is assumed to be 1.0, although in reality it is probably slightly less than 1.0 since the data was taken at Notre Dame, which is slightly higher than sea level. If the density ratio were slightly less than 1.0, then the hotwire data plotted in Fig. 5B would pivot backwards increasing the slope, which accounts for the small difference between the scaled hotwire data and the Lamb-Oseen modeled data. Unless noted, the ratio of aperture diameter to the vortex core diameter was always set at 10.

For the data shown in Fig. 5A, the vortex velocity fields were effectively two-dimensional in the sense that the axial velocity components were zero or very small. In reality, the tip-vortex velocity field typically includes a wake-like or jet-like axial velocity component. As such, a second database of tip-vortex optical aberrations were computed using the Lamb-Oseen model, this time with different values of the wake parameter A in Eq. (10). As shown in Fig. 6A, these data collapse onto slightly different curves when plotted against the scaling parameter of Eq. (14). To obtain the constant, 3.19, a linear system of the circulation parameter to the OPD_{RMS} was solved in a least squares sense, as the resulting system is over-determined. This indicates that the axial velocity field has a small but significant effect on the scaling of optical aberrations caused by the tip vortex.
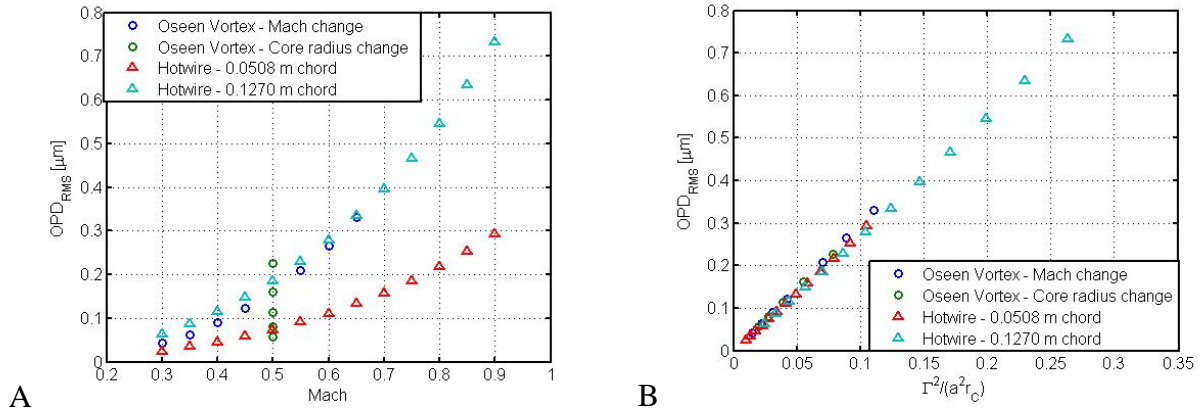

Figure 5. (A) Optical aberrations computed using the WCM for various tip-vortex parameters and, (B) the data scaled data according to Eq. (14).

To account for this effect, a second scaling relation for the optical aberrations due to the vortex axial flow field was determined by substituting the Lamb-Oseen axial-velocity relation Eq. (10) into Eq. (11), this time neglecting the radial pressure gradient, and integrating as before:

$$OPD_{RMS} \approx \left(\frac{\rho}{\rho_{SL}}\right)\frac{A^2 r_c}{a^2 x^2} \tag{16}$$

If it is assumed that the aberrations due the radial and axial velocity components are independent, then an overall scaling relation for the aberrations due to a tip vortex can be obtained by adding Eqs. (14) and (16):

$$OPD_{RMS} \approx C_1 \left(\frac{\rho}{\rho_{SL}} \right) \left(\frac{r_c}{a^2} \right) \left(\left[\frac{\Gamma}{r_c} \right]^2 + C_2 \left[\frac{A}{x} \right]^2 \right) \tag{17}$$

where C_1 are C_2 are constants that must be fit to experimental or numerical data. Figure 6B shows the same data from Fig. 6A replotted using the scaling relation Eq. (17). Figure 6B shows that the combined scaling relation, Eq. (17), collapses all of the data on to a single curve. The constant $C_1 = 3.1$ and $C_2 = 9.53$ shown in Fig. 6B were determined by minimizing the spread of the data in a least squares sense.
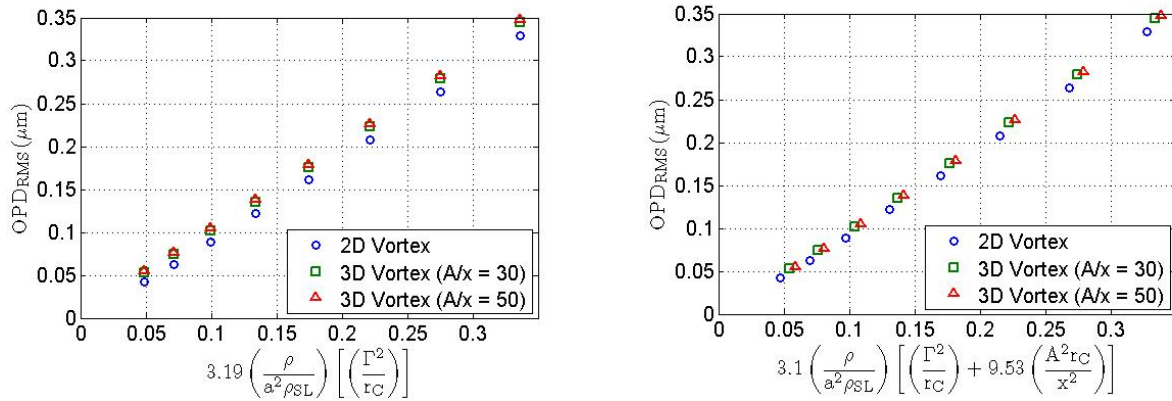

Figure 6. WCM-computed optical aberrations for tip vortices with both circumferential and axial velocity components.

Aperture Effects. As shown in Fig. 4B, the aberration produced by a tip vortex is greatest at the location of the vortex core and drops off with radial distance away from the core. As such, the effect of the aberration on a traversing beam of light depends on the diameter of the beam aperture compared to the diameter of the vortex. The beam aperture therefore acts as a spatial gain, G(AP), either increasing or decreasing the spatial OPD_{RMS} as the ratio of the vortex core to the beam aperture changes [18, 19].

The effect that the aperture diameter has on the tip-vortex aberration is investigated in Fig. 7A, which shows the OPD_{RMS} computed for the same tip-vortex flow field as a function of aperture diameter. As shown in Fig. 7A, a large amount of variability in the OPD_{RMS} exists when the size of the aperture diameter changes; however, as shown in Fig. 7B, non-dimensionalization of the aperture diameter by the vortex core diameter collapses the normalized OPD_{RMS} data onto a single curve. The curve shown in Fig. 7B can therefore be used to scale tip-vortex OPD_{RMS} data to different measurement apertures. For example, Fig. 8 shows tip-vortex aberrations computed using the WCM for different Mach numbers and beam apertures. Figure 8A shows the data without any adjustment for the aperture ratio, AP (i.e. aperture diameter to vortex core diameter), while Fig. 8B shows the same data adjusted to the same aperture ratio through the gain function $G(AP)$ shown in Fig.7B; the figure shows that scaling the data to the same aperture ratio collapses the data onto a single curve with identical OPD_{RMS}. The gain function, $G(AP)$, is the ratio of the normalized OPD_{RMS} for the value of the desired aperture ratio

to the current aperture ratio, both of which are obtained from Fig. 7B and shown in Eq (18). In Fig. 8B, all the data were adjusted to an aperture ratio of 10.

$$G(AP) = \frac{normalizedOPD_{RMS}(desired)}{normalizedOPD_{RMS}(current)} \tag{18}$$

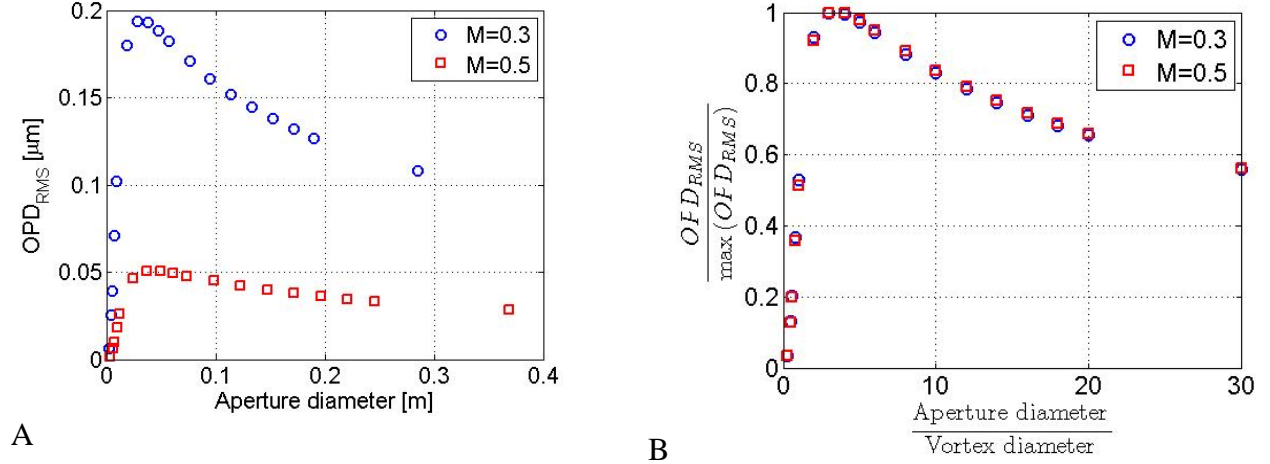A   B

Figure 7. (A) Effect of aperture diameter on the computed OPD$_{RMS}$; (B) with data non-dimensionalized.

A   B
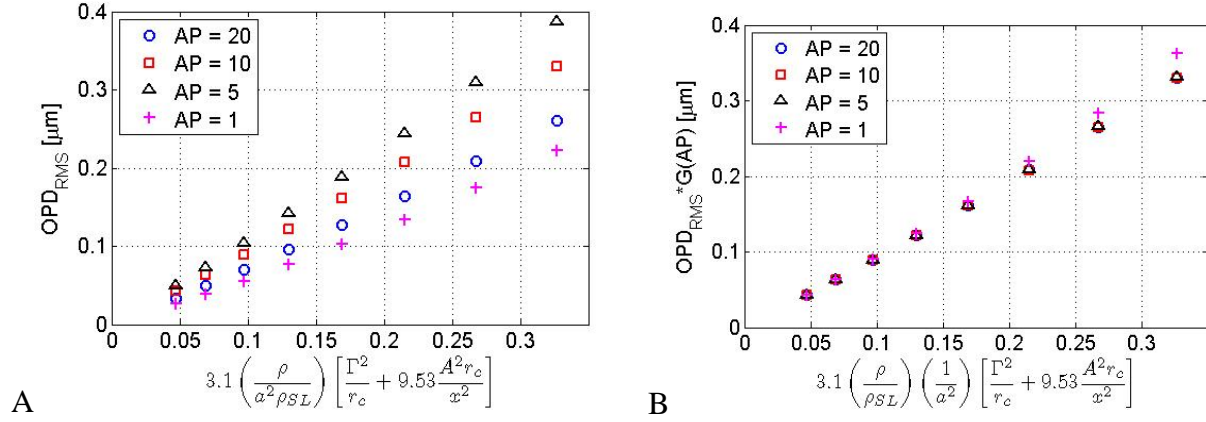
Figure 8. Correction for aperture-to-core ratio. A) Uncorrected scaling B) Corrected scaling

In summary, an overall scaling relation that includes aperture effects is shown in Eq. (19), where the aperture scaling function G(AP) is shown in Fig. 7B:

$$OPD_{RMS} * G(AP) = 3.1\left(\frac{\rho}{\rho_{SL}}\right)\left(\frac{r_c}{a^2}\right)\left(\left[\frac{\Gamma}{r_c}\right]^2 + 9.53\left[\frac{A}{x}\right]^2\right) \tag{19}$$

13

Experimental Measurements. To verify the WCM results and the scaling relation, Eq. (19), wavefront measurements using a Shack-Hartmann sensor were taken behind a half-span 60 degree delta wing. A 90 mm diameter collimated beam was sent through a 100x100 mm test section at 200 mm downstream of the trailing edge of the delta wing, see Fig. 9. The delta wing was set to three different angles of attack: 5, 10, and 15 degrees, and wavefronts were measured at Mach numbers of 0.4, 0.5, and 0.6. The test-section blockage, based on the frontal area of the wing ranged from 7 to 23%. During each test, 200 wavefronts were acquired at 10 Hz. Figure 10 shows the average *OPD* from each data set, in which tip/tilt has been removed. The trough at the center of each image is the wingtip vortex with the flow from left to right.
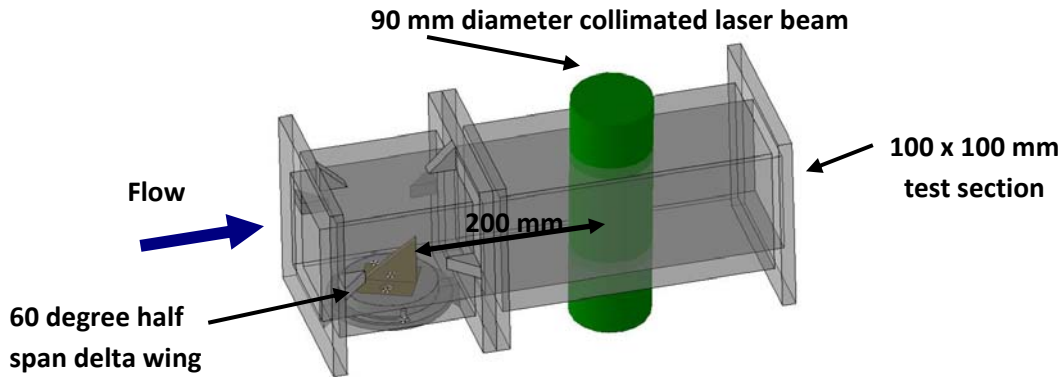

Figure 9. Experimental setup

The velocity field at the location of the wavefront measurements were also measured using a cross-wire. To obtain all three velocity components behind the delta wing the flow was surveyed twice with the cross-wire rotated by 90 degrees between surveys. All the hotwire data were taken at a freestream Mach number of 0.4 for wing angles of attack of 5, 10, and 15 degrees. The results of the cross-wire survey are plotted in Fig. 11, in which the contours represent the *u* component, and the vectors the *v* and *w* components.

The mean velocity field measured using the cross-wire was used to compute the aberration on a traversing beam of light using the WCM. Figure 12 shows that the WCM-computed OPD determined from the mean cross-wire data compares well to the mean OPD measured directly using the wavefront sensor. Figure 29 shows that the aberrations determined from both the WCM and the wavefront sensor do not approach a constant value outside of the core of the vortex, but instead fall off rapidly near the tunnel wall. This drop off is likely due to corner vortices present in the wind-tunnel test section which are clearly visible in Fig. 11. The good comparison between the WCM results and the direct wavefront measurements shown in Fig. 12 provides validation for the data and scaling relation, Eq. (19), obtained using a WCM analysis of vortex velocity fields.

5° angle of attack	10° angle of attack	15° angle of attack

Figure 10. Experimental wavefront data of the vortex behind a 60 degree half span delta wing.
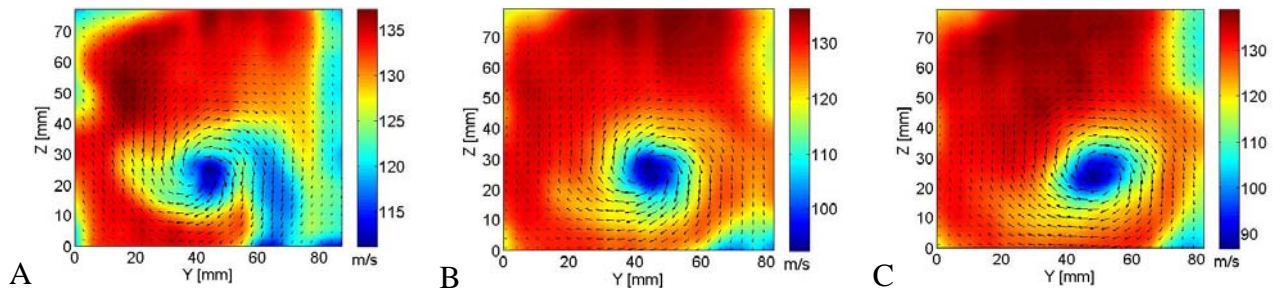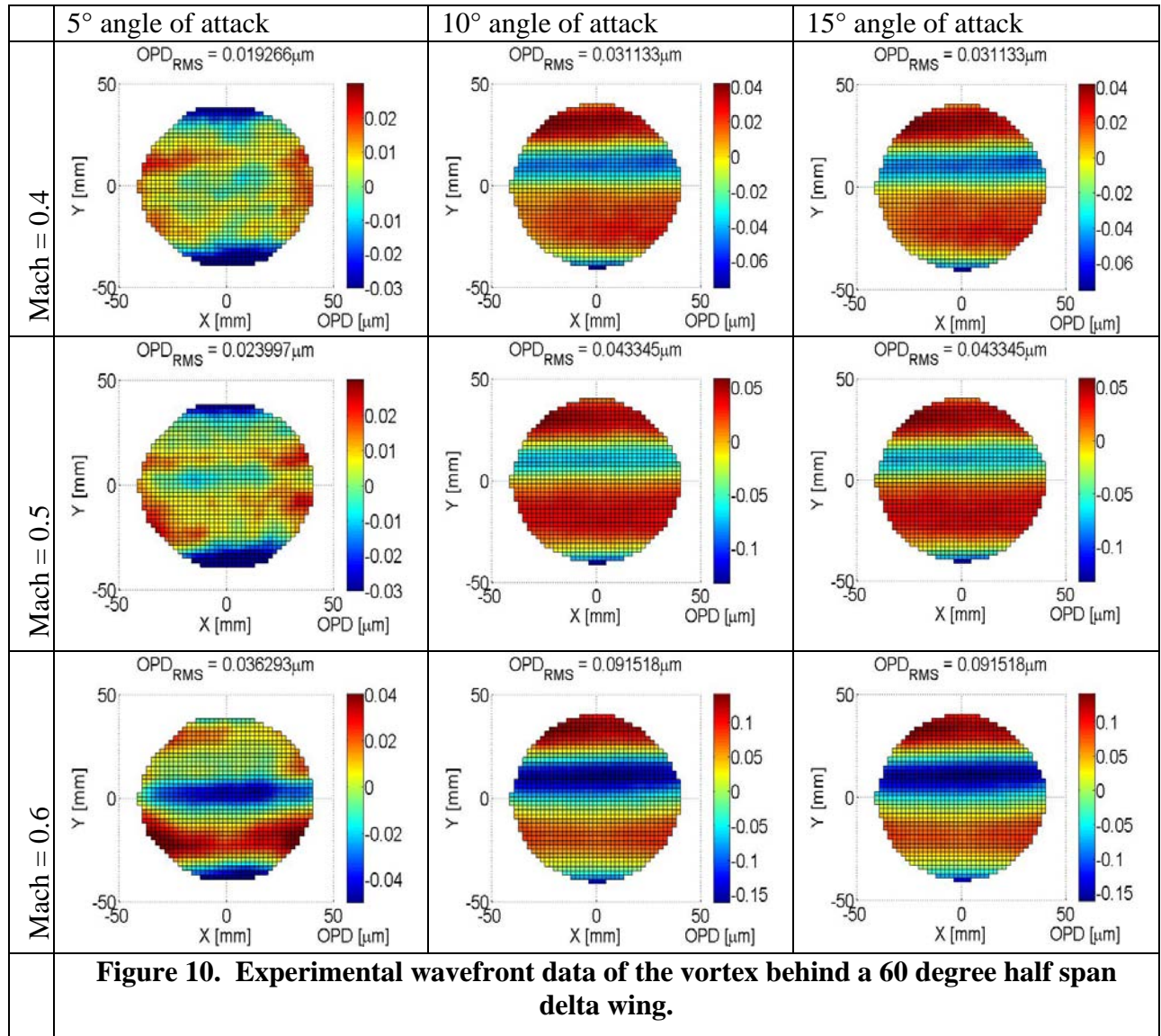

A   B   C

Figure 11. Measured velocity field behind a half-span 60 degree delta wing at Mach 0.4. A) 5 degree angle of attack B) 10 degree angle of attack C) 15 degree angle of attack
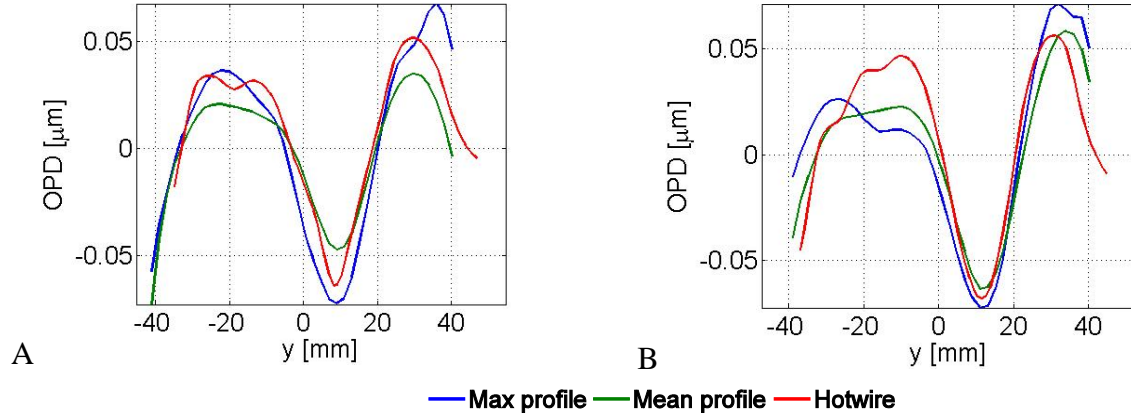
Figure 12. Comparison of measured wavefront data and WCM-computed wavefronts from cross-wire measurements behind delta wing. A) 10 degree angle of attack B) 15 degree angle of attack

The OPD_{RMS} from the direct wavefront measurements are summarized in Fig. 13A, while Fig. 13B compares these data to the curve fit determined using the WCM in conjunction with Lamb-Oseen velocity fields, Eq. (19). The figure shows that the experimental wavefront data collapse onto a single line with a slightly different slope than Eq. (19), indicating that Eq. (19) accurately models the physics of the experimental results except for a simple multiplicative constant. One possible explanation for this discrepancy is the blockage effects that the tunnel walls had on the experimental wavefront measurements which, as shown in Figs. 11 and 12, resulted in some distortion of the velocity and OPD measurements at the tunnel walls thereby making it difficult to determine accurate values of the OPD_{RMS} and vortex circulation for comparison with the model, Eq. (19). We hope to perform additional measurements of the wavefronts and velocity fields of a tip-vortex will in a wind-tunnel with larger cross section; however, Figs. 12 and 13 show that Eq. (19) still performs reasonably well for modeling tip-vortex OPD_{RMS}.
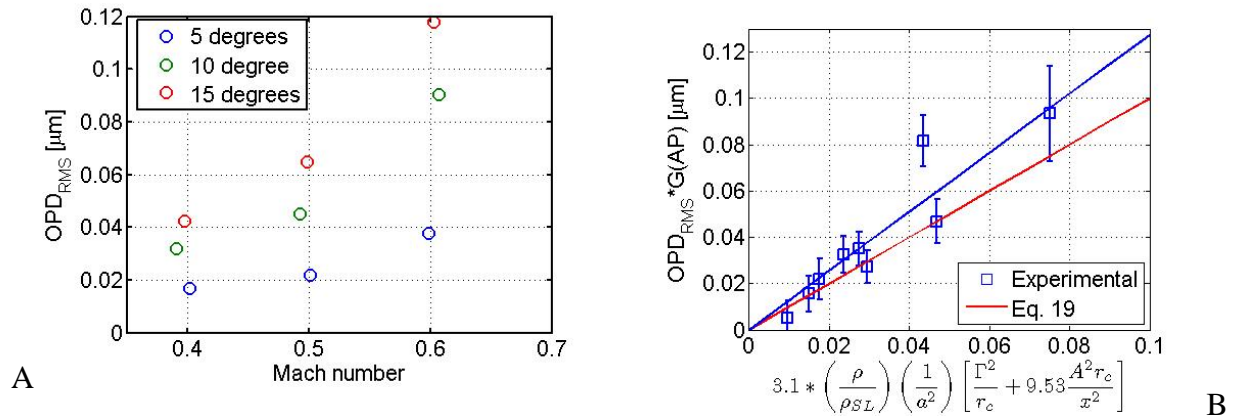

Figure 13. Measured spatial OPD behind a 60-degree half span delta wing. A) Un-scaled measured spatial OPD. B) Two-dimensional scaling based on Eq. 12 with aperture correction.

16

Full-Scale Predictions (MH-60). Using Eq. (19), predictions of the severity of the aberration from the rotor tip vortices for a full-scale helicopter were made; in this case, the helicopter chosen for the prediction was the MH-60. The strength of the tip vortices was calculated based on the weight (16680 N), number of blades (4), and assuming that all of the circulation associated with lifting the helicopter is shed into the tip vortex. The calculated blade circulation, using these parameters and assumptions was 49.8 m^2/s. Using Landgrebe's model [15], the tip vortex path was predicted using published data for hovering flight [15]. Figure 14 shows the predicted OPD_{RMS} for this configuration as a function of distance x downstream of the blade tip. For the calculations shown in Fig. 14, the axial-flow parameter A in Eq. (19) was set to 0.0 so that the case of no axial velocity in the vortex core was modeled; as such, the predictions shown here are conservative in the sense that the existence of an axial-flow velocity component would serve to increase the predicted OPD_{RMS}. Based on the Landgrebe model, the tip vortex travels approximately 150 to 200 chord lengths before it moves below the helicopter body and into the line of sight of an optical system mounted underneath the helicopter. As shown in Fig. 14, the OPD_{RMS} at a wake distance of 150 chord lengths is approximately 0.14 µm. Computation of the Strehl ratio, St, Eq. (20) for a nominal 1 µm wavelength beam gives a value of 0.46; this level of aberration, although not catastrophic, would seriously impede the ability to focus the beam on a far-field target.

$$St = \exp\left[-\left(\frac{2\pi OPD_{RMS}}{\lambda}\right)^2\right]$$
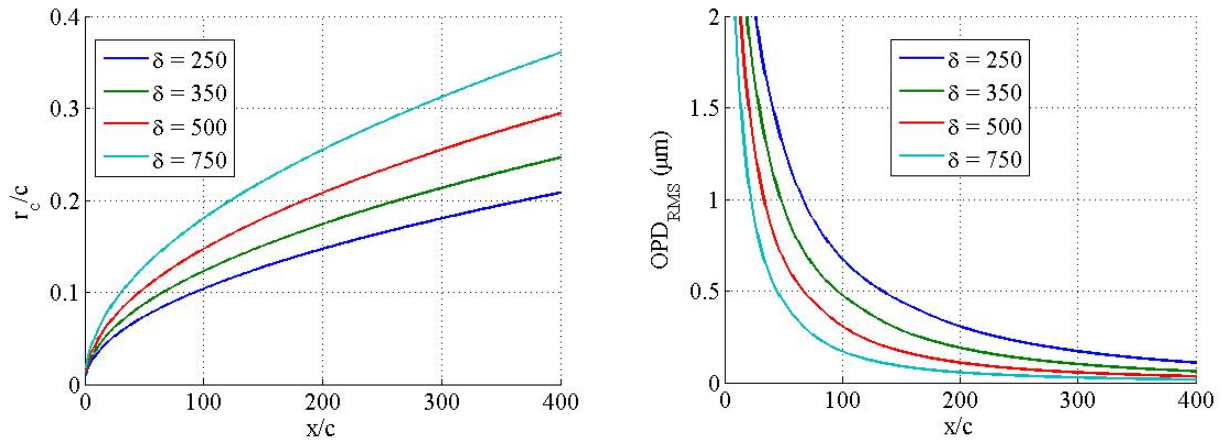
(20)

Figure 14. Predicted core radius and OPD$_{RMS}$ as a function of distance from the tip of a MH-60 helicopter blade for a 0.254 m aperture.

The results of this full-scale prediction therefore indicate that the passage of a tip vortex through the beam path would seriously degrade the far-field performance of a helicopter-mounted optical system. As shown by Fig. 14, the strength of the tip vortex aberration decays as the tip vortices move downward from the helicopter blades; however, when the helicopter is in hover, the vortex aberrations just below the body of the helicopter are still sufficiently strong to significantly

aberrate a traversing beam. This outcome has particularly serious consequences for helicopter-mounted systems if it is recognized that a belly-mounted optical system is most likely to point at distant targets by aiming just below the body of the helicopter. Finally, it should be noted that these full-scale helicopter results were estimated from published data [15], and that if the actual tip vortex radius were only slightly smaller than the aberration produced by the blade vortex system would be substantially greater. This sensitivity of the aero-optic environment to the precise helicopter flow field emphasizes the need for full-scale experimental data. Figure 15 shows how the Strehl ratio changes as a function of downstream locations for the different core growth rates shown in Fig. 14.
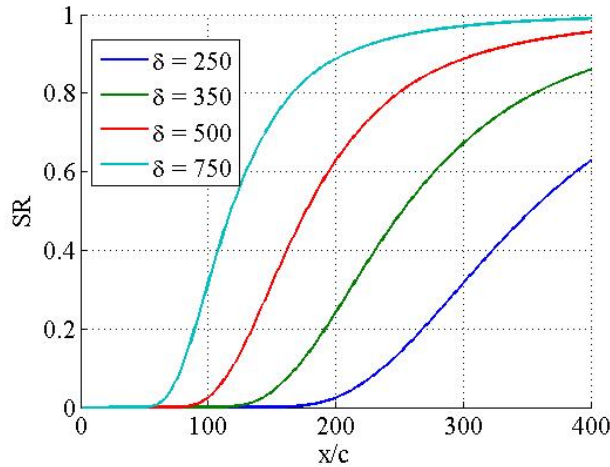

Fig 15. Predicted Strehl ratio as a function of distance from the tip of a MH-60 helicopter blade for a 0.254 m aperture.

MH_60S Flow Field Computations. In the above analysis, a single vortex in free space was modeled and centered within the aperture of the beam. No vortex interaction or induced velocity from the other blade vortices or contributions from other parts of its own vortex filament were accounted for. Therefore, any localized stagnation points from vortex interactions are not accounted for, nor is the change in pressure within the downwash slipstream, which can be calculated through a 1D momentum analysis. To account for these affects, the prescribed wake model of Landgrebe is again used for each of the four MH-60 blades. However, instead of using the scaling model as before, the Biot-Savart law is used to calculate the induced velocity throughout a single quadrant of the helicopter in hover. This flow field is then used once again with the WCM to calculate the pressure, temperature, density, and index-of-refraction throughout the flow field. Figure 16 shows the resultant pressure, temperature, and density fields for a MH-60, in which the strength of the tip vortex was set to 60 m^2/s and the core radius is set at a constant at 0.2 m. Velocity data points are spaced evenly in the x, y, and z directions at 0.08 m intervals (or 0.01R where R is the radius of the blade). This corresponds to a value of r_c/c of approximately 0.4, which is much larger than experimentation or analytic models estimate and was chosen purely for a preliminary resolution study. We hope to be able to perform further computations in a similar manner in which the core is allowed to grow much closer to what experimentation and analytical models predict. With the growth of the core radius, a finer spatial resolution must also then be obtained in the regions in which the core is small. To calculate the

pressure drop within the core of the vortex, enough velocity data points must be calculated to capture the local maximum velocity.
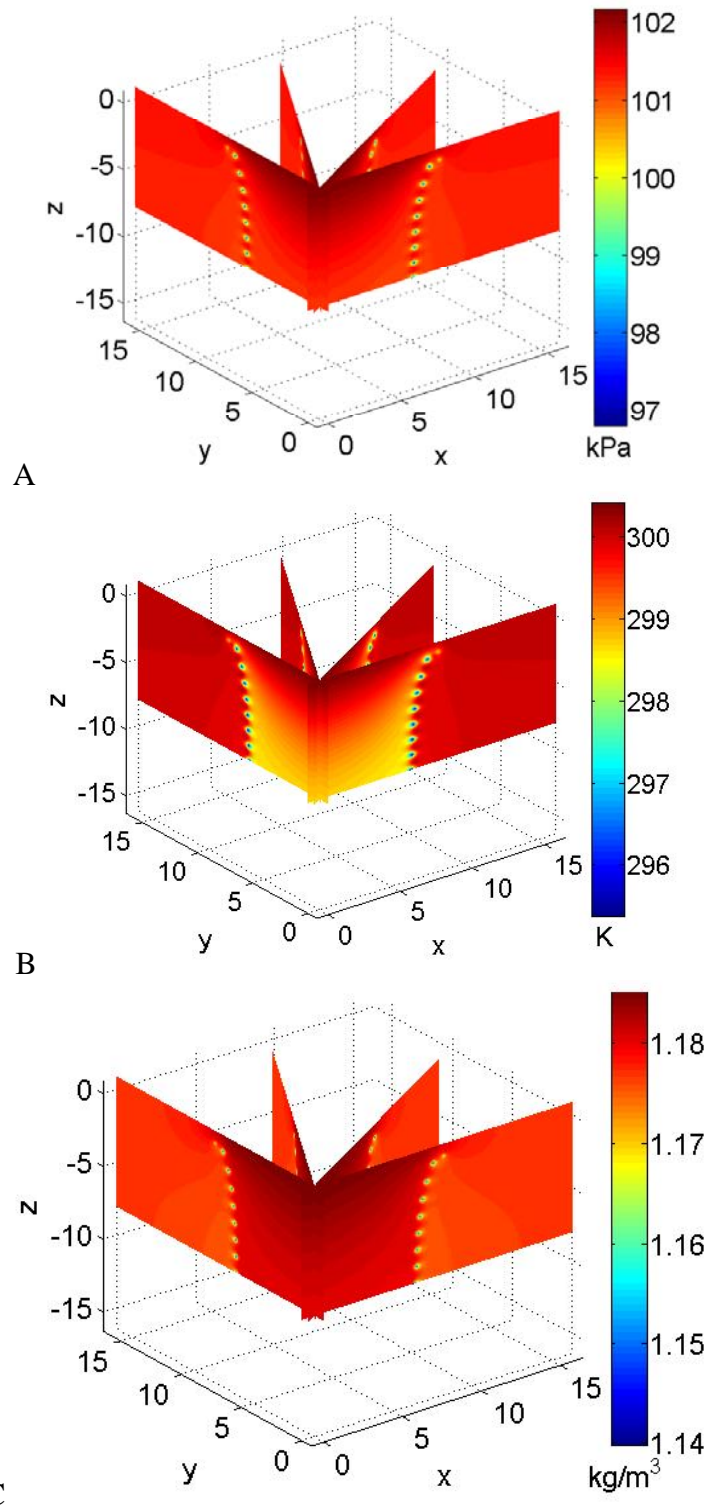

A

B

C

Figure 16. A) Pressure, B) Temperature, and C) Density fields below a MH-60 in hover.

As demonstrated through a 1D momentum analysis assuming a uniform inflow, the pressure within the slipstream, directly underneath the blades will be higher than the atmospheric pressure, which is also what the current method is calculating (Fig. 16A). Secondly, the static temperature within the slipstream is lower than the atmospheric temperature. The combination of the reduced temperature with the increased pressure results in a higher density within the slipstream. Based on geometric optics and Snell's Law, just the net change in density and therefore index-of-refraction from the slipstream to the freestream will result in the bending of light rays and consequently bore-sight error. Furthermore, the bore-sight error, ignoring the low pressure vortices passing through the system, would be a function of elevation angle as also shown by Snell's Law.

Figure 17 shows the exact same data as Fig. 16, although the blades have been represented along with the path of the tip vortices (in black). Isosurfaces of the pressure at 98 kPa are shown in blue with isocaps on the edges for everything above 97 kPa. A square 0.254 x 0.254 m^2 beam (green) is also shown at an elevation angle of zero degrees and azimuthal angle of zero degrees. The corresponding calculated wavefront with and without tip/tilt removed are also shown. As seen, tip/tilt for such a large vortex becomes the dominant Zernike polynomial, which would result in bore-sight error for such a system. Figure 18 shows the exact same data in which the azimuthal angle has been changed to 45 degrees such that the core of the vortex does not pass through the beam; the resulting wavefronts are also shown in Fig. 18. Note the large difference in the two wavefronts from Fig. 17 to Fig. 18. These changes will result in a regularly fluctuating Strehl ratio as the tip vortices pass through the beam. The spatial OPD_{RMS} of the beam passing through the vortex core is also approximately 10 times greater than the OPD_{RMS} of the beam passing between the cores. When comparing Figs. 17 and 18 the scales have changed to render the change in phase visible. Furthermore, the effect of tip/tilt has been greatly reduced creating an effective jitter as a result of fluctuating bore-sight from the cores propagating through the beam.
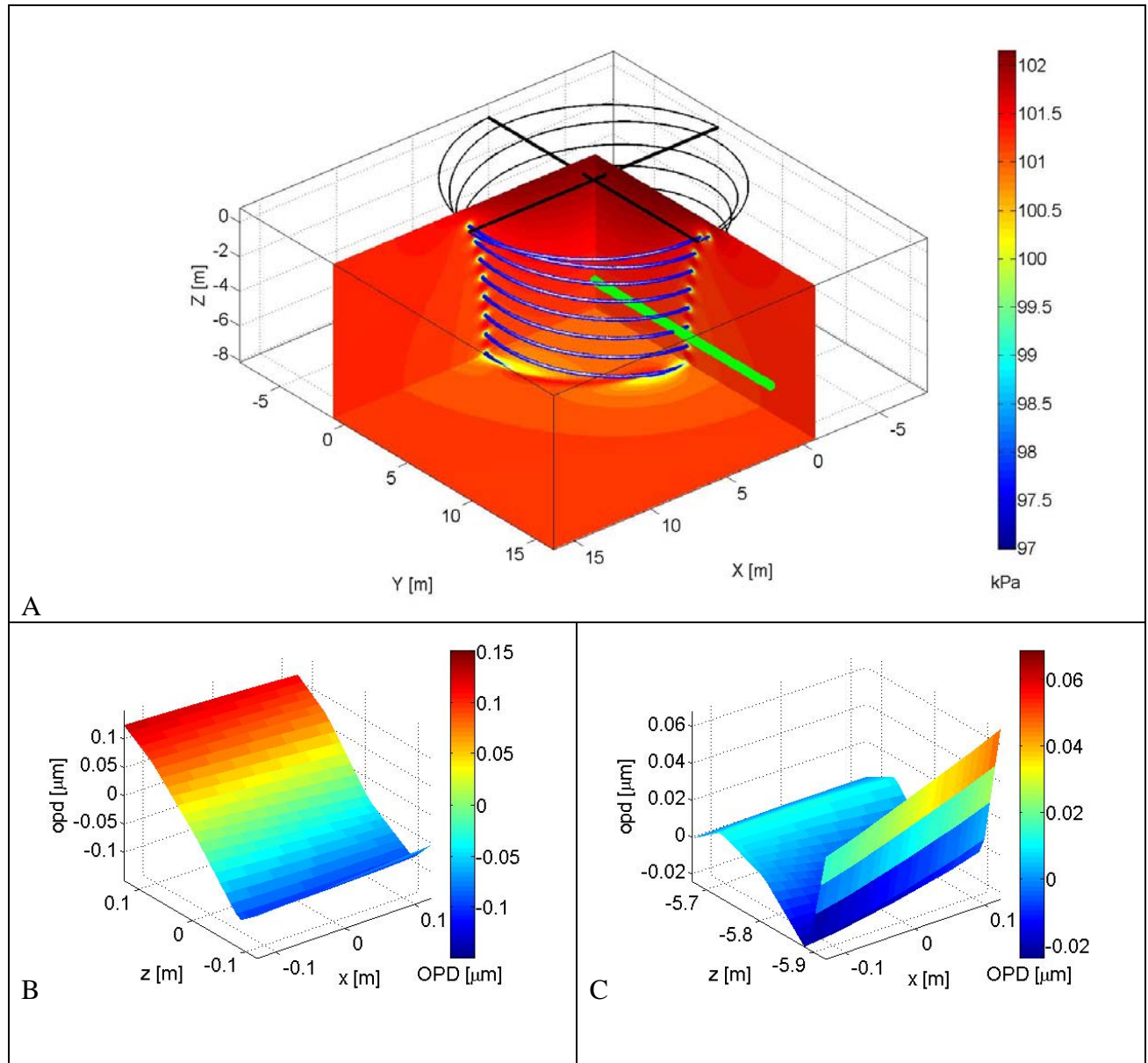
Figure 17. Rotorcraft model of a MH-60 in hover. A) Blade, tip vortex path and pressure, and optical path (El = 0, Az = 0) for a belly mounted optical system. B) Corresponding wavefront to the optical path shown without tip/tilt removed. C) Corresponding wavefront to the optical path after tip/tilt has been removed.
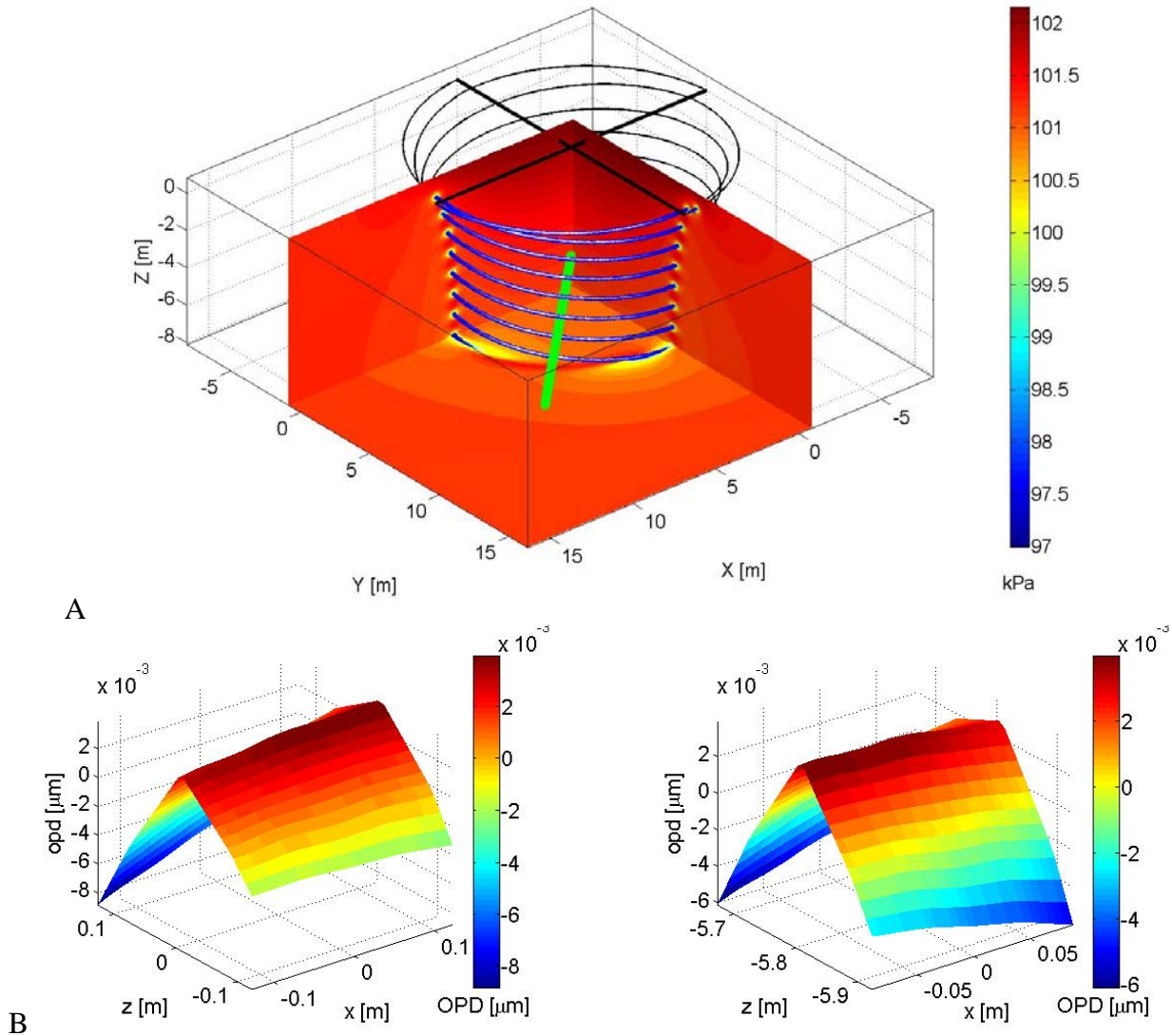
Figure 18. Rotorcraft model of a MH-60 in hover. A) Blade, tip vortex path and pressure, and optical path (El = 0, Az = 45) for a belly mounted optical system. B) Corresponding wavefront to the optical path shown without tip/tilt removed. C) Corresponding wavefront to the optical path after tip/tilt has been removed.

D. Concluding Remarks

The aberrations due to helicopter tip vortices originate from the index-of-refraction variations associated with the reduced pressure and density at the vortex core. A scaling relation has been developed from basic fluid-mechanic equations and calibrated using the Lamb-Oseen vortex model in conjunction with a thermodynamic model called the weakly compressible model (WCM). Using this calibrated scaling relation, the tip-vortex aberrations for realistic cases have been shown to be sufficiently strong to significantly impair the performance of an optical system mounted below the body of a typical helicopter.

The flow field around a MH-60 in hover has been calculated using a prescribed wake model in conjunction with the Biot-Savart law. With the velocity field calculate the weakly compressible model is used to calculate the pressure, temperature, density, and index-of-refraction fields. Once the index of refraction field is know, the wavefront of an optical beam traversing the field at any elevation and azimuthal angle combination may be calculated. To obtain pseudo-time resolved wavefronts, the velocity field for different blade positions may be calculated, yielding both a bore-sight error as a function of time as well as the resulting Strehl ratio as a function of time.

It should be stressed that this work is in its preliminary stage and we hope to have an opportunity to continue the work. If we have that opportunity, our future efforts will be directed at confirming the results obtained thus far. These efforts will consist of additional experimental measurements in a high-speed wind tunnel with lower model blockage and larger signal to noise ratios. Additional computations of the tip-vortex path for different flight regimes such as forward flight, or ground effect may also be calculated, generating a data base of index-of-refraction fields to study the aero-optic environment around the MH-60. The current hovering model relies on brute force methods as the spacing between data points is constant and therefore must be small enough to resolve the vortex cores. As a result a lot of computation resources are put into calculating a fine grid in the effective freestream where that resolution is not need. This results in a need for larger amounts of memory as well as additional computational time. New methods of using variable grid spacing in cylindrical coordinates are being investigated such that a high density of data points may be placed near the vortex filaments, with a sparse spacing elsewhere.

II. Aero-Optic Design of F/A-18 High-Energy Laser Pod

This section summarizes progress in the design of a high-energy laser pod for the F/A-18. In the previous progress report [20] it was shown that aero-optically aberrating flows could be prevented or mitigated using a fence to guide the flow around the beam aperture. The concept is illustrated in Fig. 19, which shows a fence projecting from the turret ball around the beam aperture. The fence is shaped to diffuse the flow around the top of the turret ball, thereby increasing the critical Mach number at which shock formation occurs. The fence is also shaped to contract the flow on the aft side of the turret ball, thereby increasing the flow velocity in this region in order to delay flow separation. As shown by the computational fluid-dynamic (CFD) results in Fig. 20, this improved cutout and fence design results in a more favorable pressure distribution on the turret ball with higher critical Mach number. Additional CFD studies [20] were performed for different look-back angles (Fig. 21), which showed that the adverse pressure gradient on the aft part of the turret ball was less severe with the fence than the pressure gradient leading up to flow separation on an unmodified spherical turret (Fig. 22); this result indicated that the fence would also successfully prevent or delay flow separation around the beam aperture.
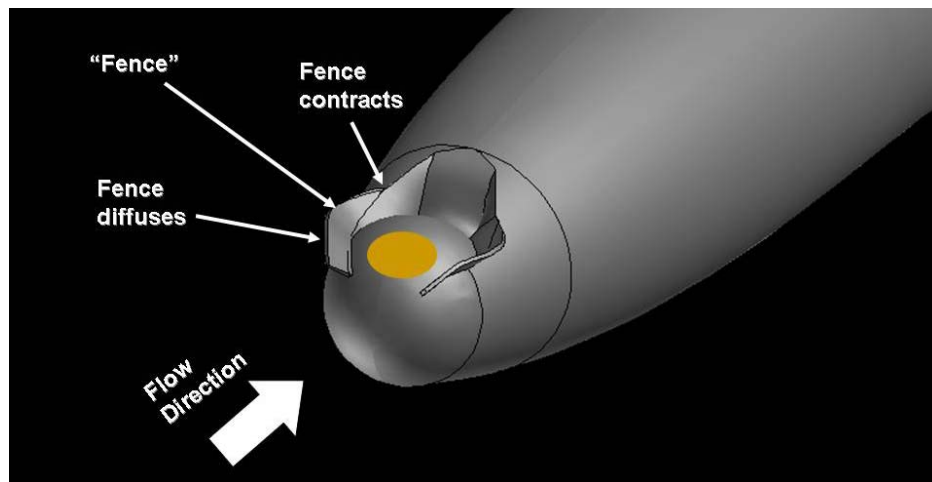

Figure 19. Pod with improved cutout and fence shaping.

A. Wind Tunnel Tests

All of the results shown in Figs. 19 to 22, including the fence shaping, were developed using CFD studies. In particular, these CFD investigations used Euler routines which did not account for viscous effects. To verify the CFD studies, a model of the pod was made and tested in the subsonic wind tunnel facilities at the University of Notre Dame. The objective of these initial low-speed wind-tunnel tests was to verify the CFD-generated pressure results, and to investigate boundary-layer and other viscous-flow effects around the pod; higher-speed measurements of aero-optical aberrations are planned in Notre Dame's Mach 0.6-capable high-speed tunnel at a later date.
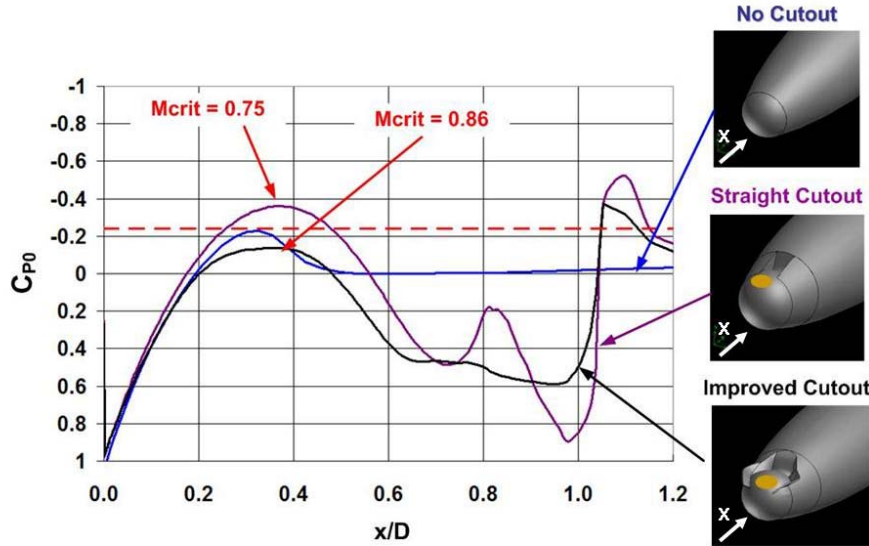
Figure 20. CFD-computed pressure distributions along cutout centerline (D = turret ball diameter) and critical Mach numbers for different configurations. "Straight" and "Improved" Cutout configurations are designed for a maximum look-back angle of 20° [19]
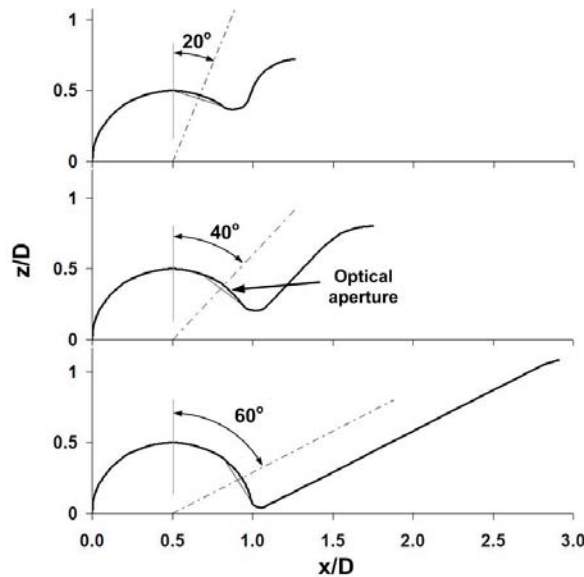

Figure 21. Contour along cutout centerline for 20°, 40° and 60° look-back angles. (D = turret ball diameter).

The Notre Dame subsonic wind tunnels have interchangeable test sections with cross sections of 2' x 2'. To keep wind-tunnel blockage within acceptable bounds, the pod model was scaled around a 6-inch diameter turret ball; furthermore, only the top half of the pod was modeled based on CFD studies which showed that accurate flow around the turret ball can still be achieved using a half model. The tests were performed at a wind speed of 45 m/s, giving a Reynolds Number based on the turret-ball diameter of roughly 450,000. In an attempt to simulate a higher-Reynolds-number flow, the boundary layer on the turret ball was tripped using a wire

with a diameter of approximately 1 mm that was mounted on the upstream side of the turret ball; this method was shown in previous studies at the University of Notre Dame to generate a realistic flow on a 6-inch diameter turret model.
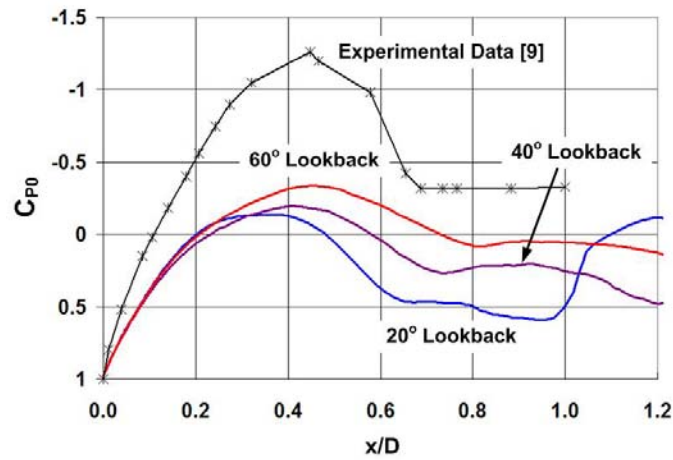

Figure 22. Comparison of CFD-computed pressure distributions for the cutouts shown in Fig. 3 to experimental data for a hemisphere-on-cylinder turret [6].

The model was mounted on a ground-plane to eliminate the upstream wind-tunnel boundary layer, and had interchangeable sections to model different look-back angles (Fig. 21) and fence heights. A diagram of the pod model and a schematic of the wind-tunnel test layout are shown in Fig. 23.
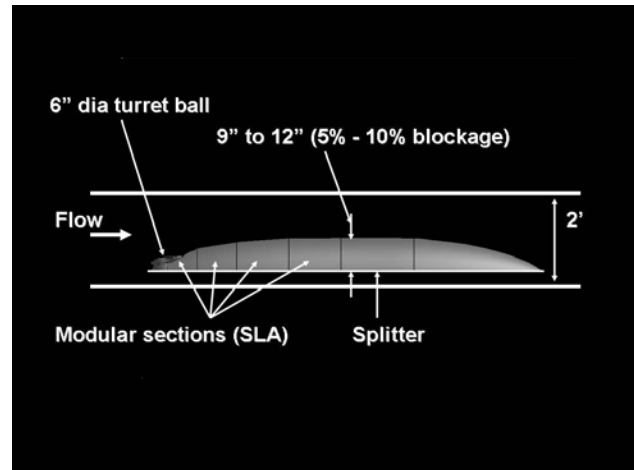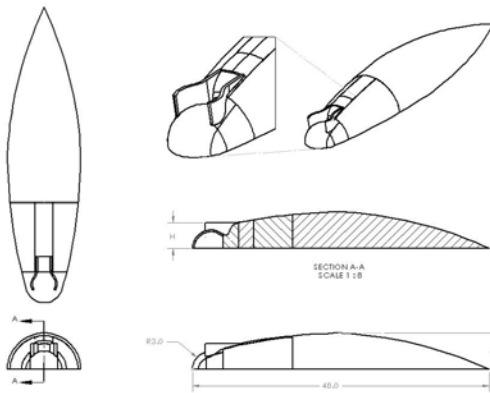

Figure 23. Drawing (left) of pod model for wind-tunnel tests, and schematic of wind-tunnel test layout (right) [20].

B. Pressure Measurements

Pressure measurements were made for three different look-back angles (20, 40, and 60 degrees, see Fig. 21), and using three different non-dimensional fence heights (corresponding to 0.7, 0.83 and 0.95 times the turret ball diameter D). The pressure data were used to compute pressure coefficients as follows:

$$Cp_i = \frac{P_i - P_s}{P_t - P_s} \qquad (1)$$

where P_i are the model surface pressures, and P_s and P_t are the freestream static and total pressures measured using a pitot-static probe mounted in the wind-tunnel test section. The pressure coefficients determined using Eq. (1) were considered "uncorrected" in the sense that the model pressures P_i were affected by wind-tunnel wall blockage effects, while the probe pressures P_s and P_t were influenced by the pressure field of the downstream pod model. It should be noted, however, that the objective of the pressure measurements was to verify the accuracy of the CFD (Euler) results. As such, rather than attempting to correct the experimental data for these blockage effects, equivalent CFD results were computed that incorporated precisely the same wind-tunnel and probe blockage effects, and used to determine equivalent "uncorrected" CFD pressure-coefficient data. It can then be presumed that, if the blockage-affected wind-tunnel and CFD results compare closely, then the performance of the pod in blockage-free conditions would also compare well with the equivalent blockage-free CFD results shown in Figs. 20 and 22.

A comparison of "uncorrected" experimental and CFD Cp distributions is shown in Fig. 24, for the pod model using a medium fence height of 0.83 ball diameters, and configured for a 40 deg look-back angle. The large excursion in the experimental Cp distribution near the front of the pod is caused by the boundary-layer trip, while the large pressure peak in the vicinity of x/D ~ 1.5 is caused by the relatively-sharp edge where the ramp at the back of the cutout blends into the downstream pod body; due to slight discrepancies in the experimental and CFD models, the pressures in this region do not compare closely. Besides these discrepancies, Fig. 24 shows that the "uncorrected" experimental and CFD Cp distributions match very well around the turret ball and in the slot region. In particular, the close match between the experimental and CFD results around the top of the turret ball (x/D ~ 0.4) indicates that the fences are successfully slowing down the flow in this region. The effect of the fences in reducing the maximum speed around the top of the ball is also clearly shown in Fig. 25, which shows experimental pressure distributions with and without the fences installed.
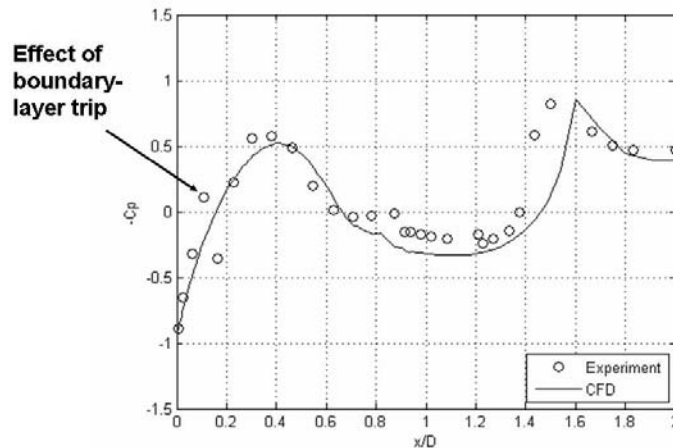

Figure 24. Wind tunnel data compared to CFD data with blockage effects, for 40 degree look-back angle and "medium" fence height

At present, CFD results that include wall blockage effects were only determined for the configuration shown in Fig. 25; however, the experimental *Cp* distributions for all of the tested configurations are summarized in Fig. 26. All of the results show that the higher fence height has a greater effect on the *Cp* distributions than the lower fence height.
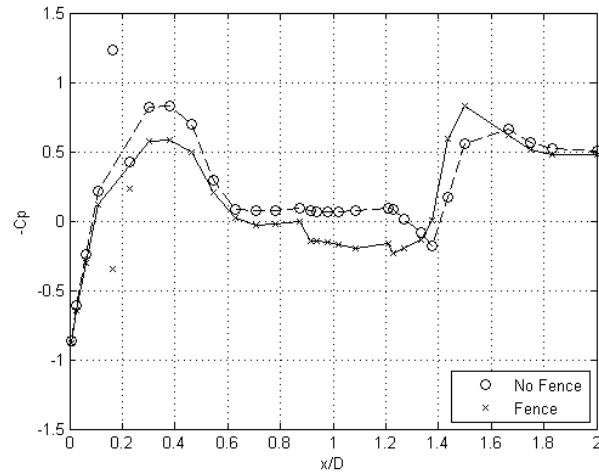

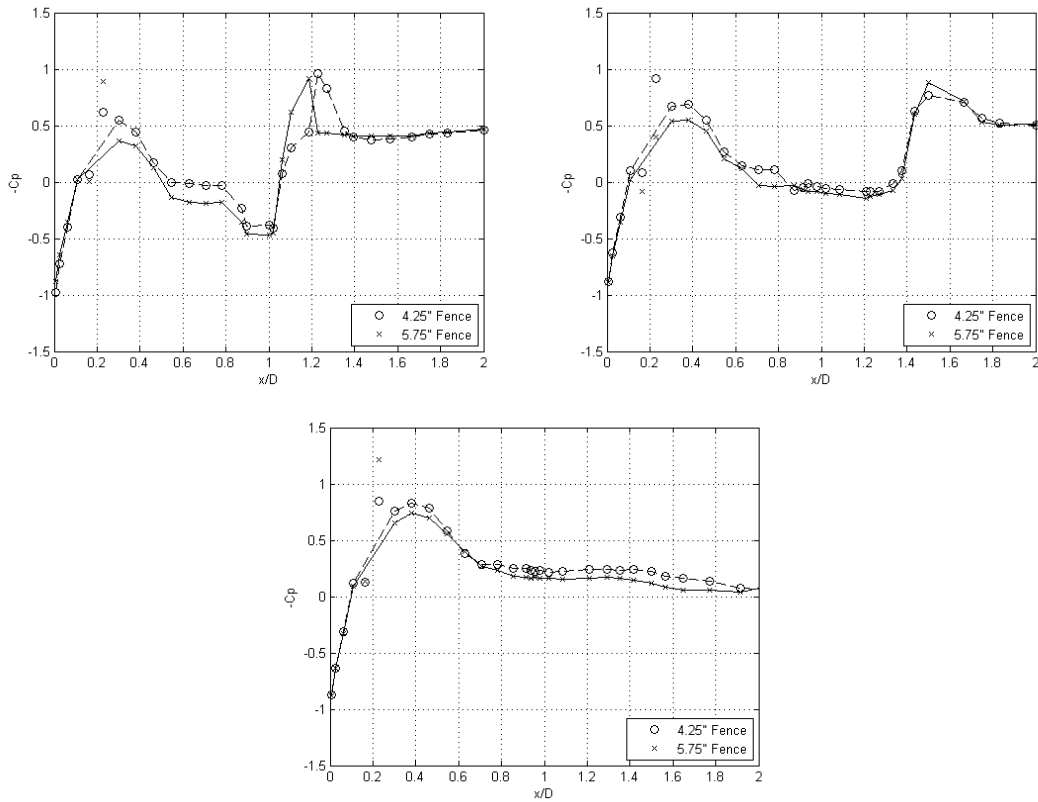**Figure 25. Measured Cp distributions with and without the fences installed.**

Figure 26. Summary of wind tunnel results for look-back angles of 20 degrees (left), 40 degrees (right) and 60 degrees (bottom).

C. Flow Visualization Results

Oil-flow visualization tests were performed using a mixture of motor oil, alcohol, liquid soap, and a dye that fluoresced under ultraviolet illumination. The liquid was applied in the vicinity of the upstream spherical turret of the pod and a black light was used to illuminate the oil traces after running the wind tunnel. In all of the flow-visualization figures shown here, the flow is going from right to left. Fig. 27 shows oil-flow pictures for the pod with the fences removed. As can be seen, there is a large accumulation of fluid just downstream of the top of the spherical turret, indicating flow separation in this region. The second puddle of fluid on the left is the lowest point of the ramp where the fluid has accumulated due to gravity.

Figure 27. Oil-flow visualization on the pod with fences removed, 40 degree look-back angle.
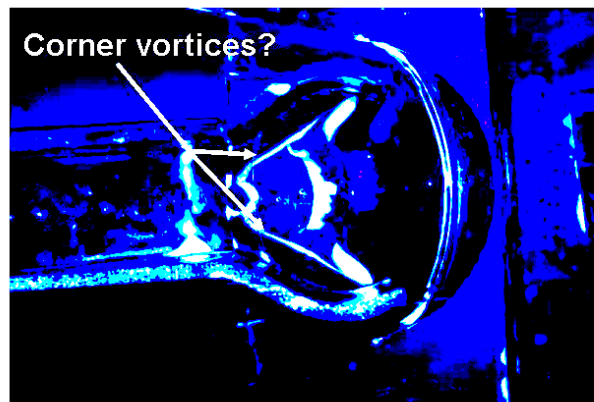

Figure 28. Oil flow visualization on the pod for 40 degree look-back angle, high fence.

An equivalent oil-flow visualization with the fences installed is shown in Fig. 28. The figure also shows an accumulation of fluid just downstream of the top of the turret ball that may indicate flow separation. Furthermore, lines of oil can clearly be seen running from each fence diagonally across the downstream half of the ball and joining at the back of the ball; these diagonal lines may indicate the existence of vortices that form in the corner between the fence and the turret surface. Overall, the flow visualization tests show that the flow over the surface of the spherical turret is noticeably affected by viscous flow effects.

Additional flow-visualization tests also indicated that the flow may not be fully attached to the inner surface of the fence walls. Flow separation from the inner surface of the fence would reduce the effectiveness of the fence in controlling the flow over the turret ball. It was hypothesized that the flow was likely separating from the relatively sharp leading edges of the fences, an effect that would be exacerbated by the low Reynolds number of the tests.
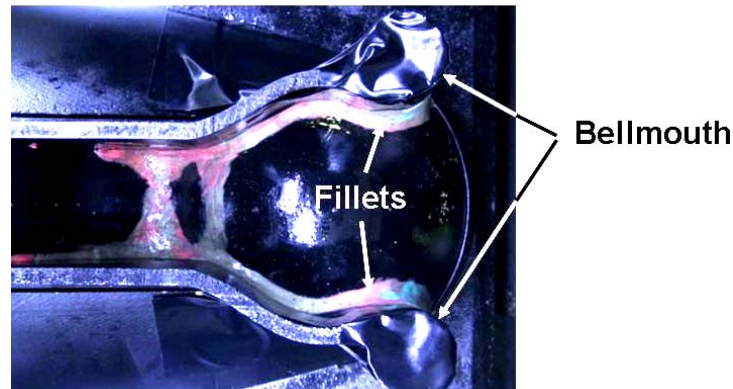

Figure 29. Photograph showing model with bell-mouth and fillet modifications.

Based on these results, the model was modified by molding plasticene fillets into the corners between the fences and the turret ball surface. Furthermore, in order to help "guide" the flow on to the inner surface of the fences, bell-mouths constructed from 1 inch diameter cylinders were attached to the leading edges of the fences. A photograph of the modified pod model, with fillets and bell-mouth, is shown in Fig. 29. It should be noted that the modifications shown in Fig. 29, particularly the bell-mouth cylinders, are sized for the conditions of the small-scale wind-tunnel tests which have a fairly low Reynolds number; it is obvious that the large bell-mouth shown in Fig. 29 would not be scaled up to a full-scale pod model.

Flow visualization for the modified model is shown in Fig. 30. As shown in the figure, the model modifications appear to have removed the possible flow separation shown in Fig. 28; however the oil flow still appears to show corner vortices originating from the fences and growing diagonally across the back surface of the turret ball. Additional testing, as well as CFD simulations, are currently being undertaken to better understand the flowfield near the inner fence walls.
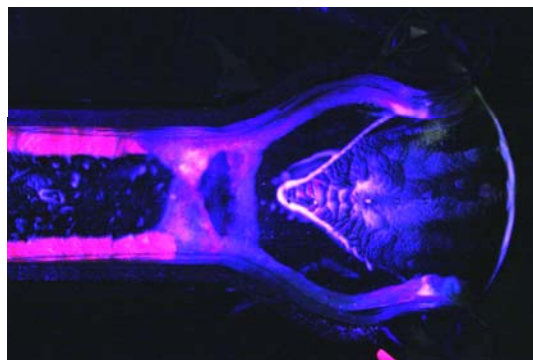

Figure 12. Surface flow visualization on the pod with the fence, plasticene fillets, and bell-mouth.

D. Summary and Future Work

This effort represents the discovery of an approach to both raising the critical Mach number of an airborne platform on which the pod is mounted so that shocks will not appear over the exit pupil of the laser and avoiding separation so that the laser's field of regard can be maximized. To our knowledge, our approach of using the virtual duct has never been proposed. Although this discovery was made using simple Euler-code analyses, the initial wind-tunnel results have shown that the virtual duct, for the most part, performs as predicted by the CFD/Euler studies [20]. In particular, the surface pressure data show that the fences significantly lower the maximum (negative) Cp of the turret ball, and compare closely to CFD-computed pressure distributions that include the same blockage effects. Flow-visualization tests indicate, however, the existence of what appear to be vortices originating in the corners between the fence walls and the turret surface. The exact nature of the flow in this region has thus far proven difficult to determine by smoke or oil-flow visualization tests.

If this work continues, future efforts will be directed towards viscous CFD studies using RANS or detached-eddy simulations in order to better identify the cause of the observed oil-flow results. These studies will be run at low-Reynolds numbers comparable to the Reynolds numbers associated with the wind-tunnel results obtained thus far. Equivalent CFD calculations will also be run at high Reynolds numbers corresponding to full-scale flight, to evaluate whether the viscous flow effects observed in the wind-tunnel will also exist in full-scale flight conditions, or whether they are an anomaly of the low Reynolds number associated with the wind-tunnel tests.

Future work will also include testing at lower blockages in the University of Notre Dame's 3-foot Wind Tunnel, eventually leading to optical measurements. Finally, additional work on the fence shape is planned; the objective of this work will be to attempt to determine the best fence shape using design-optimization techniques [22].

III. High bandwidth Shack-Hartmann wavefront sensor

A new analog 2-D high-bandwidth Shack-Hartmann wavefront sensor (SHWFS) was designed capable of acquiring data at greater than 100 kHz temporal rate, in addition to a spatial resolution of one-tenth of the aperture. This novel sensor can be used to address high temporal bandwidth aero-optical aberrated flows that cannot be addressed by the currently available state-of-art wave front sensors. Progress on the sensor was covered extensively in an earlier report [20] and has been documented in two papers [23,24]. The only portion of this work not previously reported is that the sensor has now been mounted in an enclosure and is now being used to record unsteady wavefront data.

Reference

[1] Gordeyev, S., and Jumper, E.J., "Aero-Optical Characteristics of Compressible Subsonic Turbulent Boundary Layers," AIAA-2003-3606, June, 2003.

[2] Rennie, R. M., Siegenthaler, J. P., and Jumper, E. J., "Forcing of a Two-Dimensional, Weakly-Compressible Subsonic Free Shear Layer," AIAA 2006-0561, Jan., 2006.

[3] Gordeyev, S., Hayden, T., and Jumper, E., "Aero-Optical and Flow Measurements Over a Flat-Windowed Turret," *AIAA Journal*, Vol. 45, No. 2, 2007, pp.347-357.

[4] Gordeyev, S., Post, M.L., McLaughlin, T., Ceniceros, J., and Jumper, E.J., "Aero-Optical Environment Around a Conformal-Window Turert," *AIAA Journal*, Vol. 45, No. 7, 2007, pp.1514-1524.

[5] Rennie, R.M., Duffin, D.A., and Jumper, E. J., "Characterization and Aero-Optic Correction of a Forced Two-Dimensional, Weakly-Compressible Subsonic Free Shear Layer," *AIAA Journal*, Vol. 46, No. 11, 2008, pp.2787-2795.

[6] Gordeyev, S., Post, M.L., McLaughlin, T., Ceniceros, J., and Jumper, E.J., "Aero-Optical Environment Around a Conformal-Window Turert," *AIAA Journal*, Vol. 45, No. 7, 2007, pp.1514-1524.

[7] Devenport, W., Rife, M., Stergios, L., and Gordon, F., "The structure and development of a wing-tip vortex", J Fluid Mech (1996) 326:67-106.

[8] Iungo, G., Skinner, P., and Buresti, G., "Correction of wandering smoothing effects on static measurements of a wing-tip vortex", Exp Fluids (2009) 46:435-452.

[9] Green, S. I. and Acosta, A. J., "Unsteady flow in trailing vortices," J Fluid Mech (1991) 227:107-134.

[10] Rossow, V. J., "Lift-generated vortex wakes of subsonic transport air," Progress in Aerospace Sciences (1999) 35: 507-660.

[11] Zang, H.J., Zhou, Y., Whitelaw, J.H., "Near-Field Wing-Tip Vortices and Exponential Vortex Solution," J Aircraft (2006), Vol. 43, 2:445-449.

[12] Papamoschou, D., and Roshko, A., "The compressible turbulent shear layer: an experimental study," *Journal of Fluid Mechanics*, Vol. 197, 1988, pp. 453-477.

[13] Fitzgerald, E.J. and Jumper, E.J., "The Optical Distortion Mechanism in a Nearly Incompressible Free Shear Layer," *Journal of Fluid Mechanics*, 512, 2004, pp. 153-189.

[14] Babie, B. M., "An Experimental and Analytical Study of the Stability of Counter-Rotating Vortex Pairs with Applications for Aircraft Wake Turbulence Control," Ph.D. Dissertation, Aerospace and Mechanical Engineering Department, Univ. of Notre Dame, Notre Dame, IN, April 2008.

[15] Leishman, J. G., "Principles of Helicopter Aerodynamics," Cambridge Aerospace Series (2000).

[16] Gordeyev, S. and Jumper, E., "Aero-Optics Characteristics of Compressible, Subsonic Turbulent Boundary Layers," 34th AIAA Plasma Dynamics and Lasers Conference, 2003, AIAA 2003-3606.

[17] Vitistas, G. H., "The Optics of the Compressible N=2 Vortex," Transactions of the CSME/de la SCGM, Vol. 30, No. 1, 2006.

[18] Seigenthaler, J., Gordeyev, S., and Jumper, E. J., "Shear Layers and Aperture Effects for Aero Optics," AIAA-2005-4772, June, 2005.

[19] Siegenthalar, J., "Guidelines for Adaptive-Optic Correction Based on Aperture Filtration," Ph.D. Dissertation, Aerospace and Mechanical Engineering Department, Univ. of Notre Dame, Notre Dame, IN, December 2008.

[20] Rennie, R. M., and Jumper, E. J., "Annual Report to ONR: Aero-Optical Investigation of a Pod Directed Energy System," University of Notre Dame, Feb 2009.

[21] Rennie, R. M., Crahan, G., and Jumper, E. J., "Aerodynamic Design of an Aircraft-Mounted Pod for Improved Aero-Optic Performance," AIAA Paper 2010-0437, Jan, 2010.

[22] Gano, S.E., and Renaud, J.E., "Hybrid Variable Fidelity Optimization Using a Kriging-Based Scaling Function," *AIAA Journal*, Vol. 43, No. 11, 2005, pp. 2422-30.

[23] Abado, S., Gordeyev, S. and Jumper, E. J., "Designing and Testing a New Shack-Hartmann High Bandwidth Two-Dimensional Wavefront Sensor," AIAA Paper 2009-4225 (2009).

[24] Abado, S., Gordeyev, S. and Jumper, E. J., "Designing and testing a high-bandwidth 2-D wavefront sensor for aero-optics," Proc. SPIE, Vol. 7466, 746602 (2009).